Research

CrossMark
click for updates

Author for correspondence:
Francois Barthelat
e-mail: francois.barthelat@mcgill.ca

An improved failure criterion for biological and engineered staggered composites

Francois Barthelat, Ahmad Khayer Dastjerdi and Reza Rabiei

Department of Mechanical Engineering, McGill University, 817 Sherbrooke Street West, Montreal, Quebec, Canada H3A 2K6

High-performance biological materials such as nacre, spider silk or bone have evolved a staggered microstructure consisting of stiff and strong elongated inclusions aligned with the direction of loading. This structure leads to useful combinations of stiffness, strength and toughness, and it is therefore increasingly mimicked in bio-inspired composites. The performance of staggered composites can be tuned; for example, their mechanical properties increase when the overlap between the inclusions is increased. However, larger overlaps may lead to excessive tensile stress and fracture of the inclusions themselves, a highly detrimental failure mode. Fracture of the inclusions has so far only been predicted using highly simplified models, which hinder our ability to properly design and optimize engineered staggered composites. In this work, we develop a new failure criterion that takes into account the complex stress field within the inclusions as well as initial defects. The model leads to an 'optimum criterion' for cases where the shear tractions on the inclusions is uniform, and a 'conservative' criterion for which the tractions are modelled as point forces at the ends of the overlap regions. The criterion can therefore be applied for a wide array of material behaviour at the interface, even if the details of the shear load transfer is not known. The new criterion is validated with experiments on staggered structures made of millimetre-thick alumina tablets, and by comparison with data on nacre. Formulated in a non-dimensional form, our new criterion can be applied on a wide variety of engineered staggered composites at any length scale. It also reveals new design guidelines, for example high aspect ratio inclusions with weak interfaces are preferable over inclusions with low aspect ratio and stronger interfaces. Together with existing models, this new criterion will lead to optimal designs that harness the full potential of bio-inspired staggered composites.

1. Introduction

Composite materials consist of two or more different materials with complementary properties, which, when properly arranged, can lead to new and attractive combinations of properties not accessible to monolithic materials [1]. Various composite configurations are used in engineering, the most prominent being strong and stiff fibres embedded in a softer matrix. Composite materials are also common in the natural world. For example, tendon, intervertebral discs, fish scales or sea anemones are biological-fibre reinforced-composites based on collagen fibres. Another common configuration in nature is the staggered structure found in bone [2], spider silk [3], collagen fibrils [4] and nacre from seashells [5] (figure 1a). In this arrangement, stiff inclusions of high aspect ratio but finite length are assembled parallel to the direction of loading, and they overlap over some distance in order to transfer loads via shear stresses at the interfaces. When a brittle and stiff material is to be combined with a softer and more ductile matrix, the staggered structure has been identified as the most optimum configuration to achieve both high strength and high toughness [6], two properties that are usually difficult to achieve simultaneously [7]. A well-known example of a staggered composite is nacre, in which the inclusions are mineral tablets forming a brick-wall-like three-dimensional structure where softer organic materials serve as
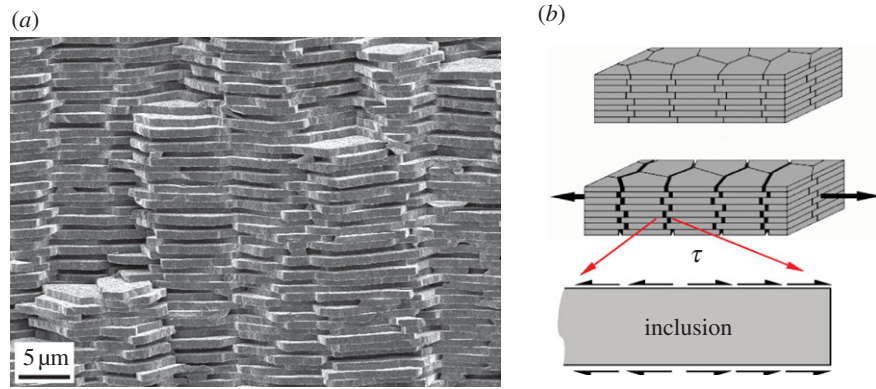
(a)

(b)

Figure 1. (a) The microstructure of natural nacre (shown here from the shell *Trochus Niloticus*); (b) Micromechanics of sliding of the inclusions generate large deformations at the microscale. In this mechanism, each inclusion is subjected to shear tractions. (Online version in colour.)

nanometres-thick mortar (figure 1b). Nacre is stiff and strong compared with other biological materials, but it is its toughness which is the most impressive; it is several orders of magnitude tougher than the mineral of which it is made [8]. Specific mechanisms such as crack bridging and process zone toughening were recently shown to be the main contributors to this tremendous amplification of toughness [8,9]. Such performance is not matched by any engineering material to this day, and, for this reason, there have been significant efforts over the past 10 years towards fabricating staggered composites [10–13]. The basic micromechanics of deformation and failure for the staggered structure can be represented by a 'tension–shear–tension' model wherein the inclusions carry tensile stress and the interfaces channel loads between inclusions via shear stress [14]. This configuration has been the basis for most models used to predict modulus and strength [2,6,15–17]. In this model, the inclusions are predominantly subjected to shear tractions from the interface as shown in figure 1b. In the ideal case, the deformation mechanism occurs by 'sliding' of the inclusions on one another once the interface shear strength is reached, which generates relatively large deformations and energy dissipation and toughness (figure 1b) [18–20]. In terms of optimizing this structure, all existing models for staggered composites predict that the modulus, strength and toughness increase with the amount of overlap between inclusions. Increasing the overlap length between inclusions however also increases the tensile stresses carried by the tablets, which may lead to the fracture of the inclusions themselves. This failure mode is highly detrimental, because it suppresses all the mechanisms of energy dissipation and toughness associated with sliding of the inclusions.

While this design limitation has been recognized for a while for natural and engineered staggered composites [21], an accurate criterion to predict the fracture of the inclusions is still missing. Typically, only the average of the tensile stress over the cross section of the inclusions is considered, and compared directly with the tensile strength of the material to predict failure [11,16,17,21,22]. This simplified criterion may lead to large errors because the stress profile across the inclusion is far from being uniform [23]. The inclusions contain stress singularities [22], which must be taken into account because they are typically brittle and highly sensitive to stress concentrations. Moreover, the simplified criterion does not incorporate size effects. To this end, Gao *et al*. [24] used a fracture mechanics-based approach

to predict the failure of inclusions in staggered composites, and in hierarchical, self-similar staggered composites [25]. In this model, a pre-existing flaw is considered in the inclusion, but its effects are simply modelled as a through crack in an infinite material in uniaxial tension. The interaction of flaws with the complex stress field within the inclusions was not considered in any of the earlier-mentioned models. In this work, we have developed an improved failure criterion that addresses the above shortcomings. We conducted experiments on small staggered structures made of alumina tablets bonded by epoxy and polyurethane, which highlight the need for an improved criterion. We then developed a new failure criterion for the inclusions subjected to uniform and non-uniform shear tractions at the interface. Our new criterion is compared with the experiments on alumina tablets and with the mineral tablets in nacre. Finally, the implication of the new criterion on the design and scaling of staggered composites is discussed.

2. Experiments

2.1. Tensile tests on staggered structures

The objective of the experiments was to capture the two different failure modes of tablet fractures and tablet sliding on small staggered structures of well-defined geometry and dimensions. The samples consisted of seven alumina tablets bonded by adhesive (figure 2a). In this configuration, the central tablet is subjected only to shear tractions from the interfaces, and it carries the largest amount of stress. The failure modes of this small structure are representative of staggered composites made of a larger number of tablets, because under the same macroscopic uniaxial tensile loading, the tablets within a staggered composite would be subjected to the same shear tractions as the central tablet in the small model. This small two-dimensional structure was therefore assumed to capture the failure modes observed in more complex three-dimensional structures, similar to the two-dimensional analytical models used to capture the salient deformation mechanisms of nacre [19,24]. For sample preparation, small tiles of aluminium oxide (CerCo LLC, OH, USA) were cut into tablets (length = 10 mm, width = 3.2 mm, thickness = 0.3–0.5 mm) using a precision diamond saw. The tablets were then assembled with engineering adhesives to form three-tablet-thick staggered structures (figure 2a). Before assembly a small amount of glass spheres
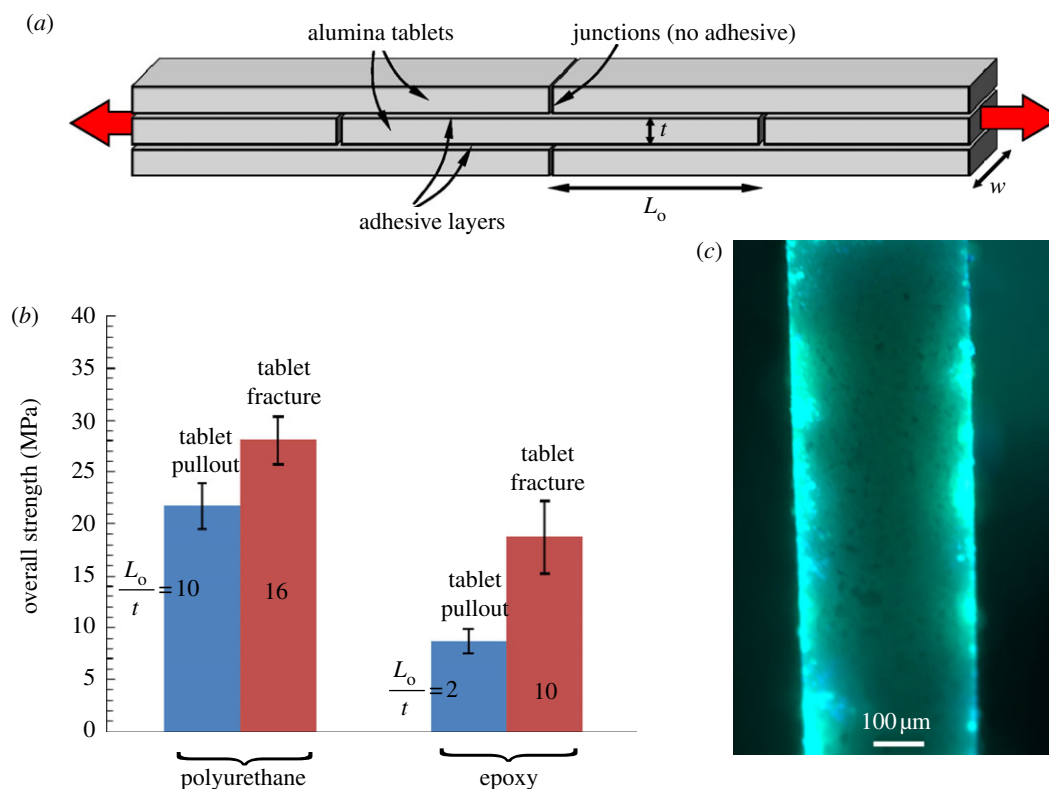
3

Figure 2. (a) Configuration of the staggered tablet tensile test; (b) overall strength for two different adhesives and two overlaps; (c) a fractured tablet imaged with fluorescent microscopy revealed pre-existing edge cracks up to 60 μm deep. (Online version in colour.)

(0.4% weight), 30 μm in diameter (Polysciences Inc., Warrington, PA, USA), was mixed with the glue in order to obtain a uniform and consistent bond line thickness. This small concentration of spheres lies within a range that does not affect the behaviour of the interface: doubling their concentration did not affect the interfacial shear strength of the interfaces. The ends of the specimen were embedded in cylindrical epoxy pucks, in which holes were drilled to apply tensile loads. The samples were tested using a miniature loading machine (Ernest F. Fullam, Inc, Latham, NY, USA) at a rate of 10 μm s^{-1}. During the tests, each sample was monitored with a camera in order to identify the failure mode. Two types of glue were used: a weak and compliant elastomeric adhesive (polyurethane, PL Premium, Lepage, Brampton, ON, Canada) and a stiff and strong thermoset adhesive (EpoThin epoxy, Buehler, Lake Bluff, IL, USA). For each glue, two different combinations of overlap length L_o and tablet thickness t were selected to fail the structure by either tablet sliding or tablet fracture. The overall strength of the structure was then computed using $\sigma_S = F_s/3tw$, where F_s is the force at failure, t is the thickness and w is the width of the tablets. The value obtained would roughly correspond to the strength of a hypothetical composite made of many of these staggered tablets. The overall strength for different combinations of glues and ratios L_o/t are shown in figure 2b. For both adhesives, small overlaps led to tablet pullout. This failure mode is identical to what is obtained from a double shear lap test [26], which can be used to compute the average shear strength of the interface $\tau_S = F_s/2L_ow$. We found $\tau_S = 8.2$ MPa for epoxy and $\tau_S = 4.5$ MPa for polyurethane. When larger overlaps were selected for each of the glues, the central strip itself fractured near the junctions (figure 2a). The apparent strength of the tablets in this configuration can be computed using $\sigma_t = F_s/tw$, where t is the

thickness of the tablets. σ_t corresponds to the maximum value of the average of tensile stress over the cross section. We found an apparent tensile strength of $\sigma_t \approx 40-90$ MPa for the alumina tablets.

2.2. Tablet strength and failure prediction

The strength of the alumina strips was also independently measured by way of four-point bending test. As expected, the strips failed in a brittle fashion, at a calculated tensile strength of 275 MPa. This value is consistent with the manufacturer's specification for that ceramic, but it is three to seven times higher than the apparent tensile strength of the tablets σ_t calculated earlier. The commonly used criterion for tablet fracture, which consists of comparing the stress averaged over the section of the tablet with the strength of the material [11,16,17,21,22,27], therefore largely overestimates the strength of the tablets in the staggered structure. This result was expected, because this simplified criterion does not take into account stress concentrations. We also compared our experimental results with another existing fracture criterion proposed by Gao et al. [24] based on fracture mechanics, which considers an initial flaw of length $2a$ within the tablets [5]. This criterion may be more appropriate because the tensile strength of brittle ceramics is governed by the size and configurations of pre-existing flaws as well as the fracture toughness. To apply this criterion, we estimated the size of initial flaws in our alumina tablets, assuming a two-dimensional configuration. The stress intensity factor for an edge crack in a beam in bending is given by [28]:

$$K_I = \sigma\sqrt{\pi a}\sqrt{\frac{2t}{\pi a}\tan\frac{\pi a}{2t}}\frac{0.923 + 0.199(1 - \sin \pi a/2t)^4}{\cos \pi a/2t}. \quad (2.1)$$
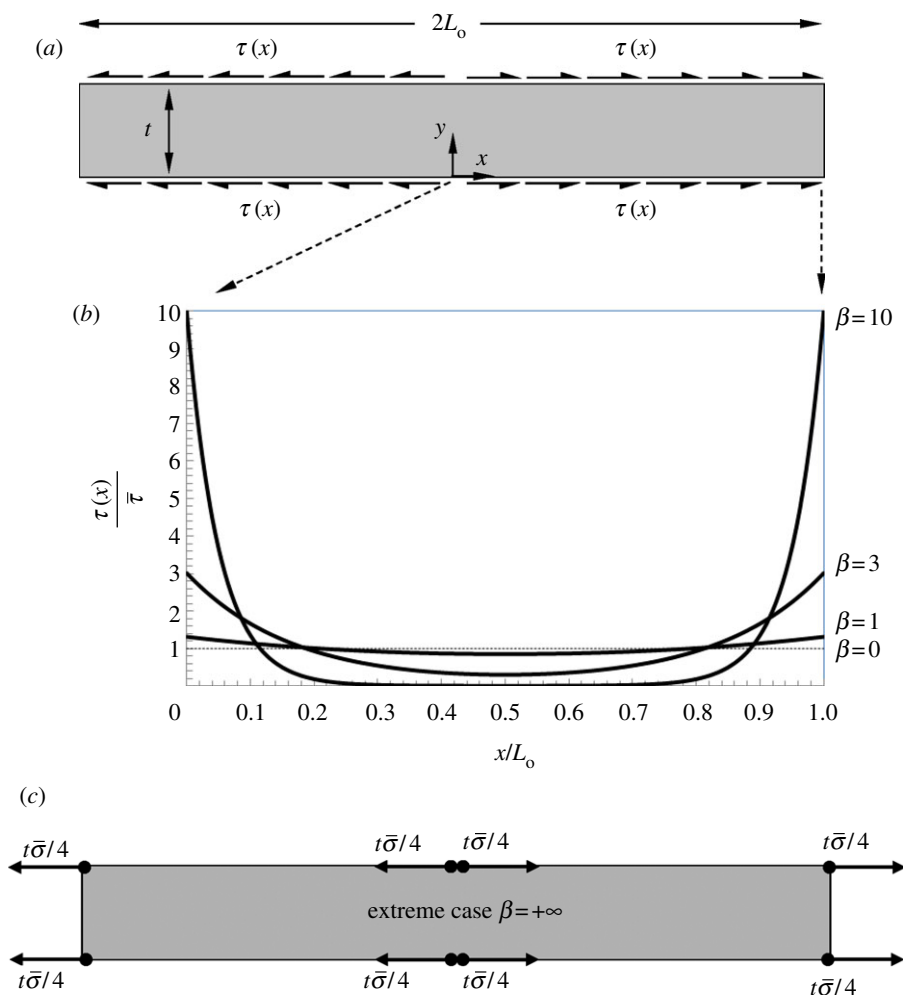
Figure 3. (a) Schematic of an inclusion subjected to shear tractions generated by the interfaces between inclusions; (b) profiles of shear traction for different values of β; and (c) extreme case where $\beta = +\infty$: the shear tractions are represented by point forces at the ends of the overlap regions. (Online version in colour.)

Using the dimensions of the samples, $K_I = K_{IC} = 3.9$ MPa.m$^{1/2}$ (fracture toughness of the alumina tablets provided by the manufacturer) and $\sigma = 275$ MPa (tensile strength measured above) leads to an edge crack length of $a = 60\ \mu$m. The size and configuration of the flaws were also verified by direct observation. A group of alumina tablets was soaked in a fluorescent dye for 24 h, after which the tablets were fractured. The fracture surfaces were imaged using a fluorescent microscope, and the green dye revealed the configuration and size of pre-existing cracks consisting of edge cracks about 60 μm deep (figure 2c). Gao's criterion for inclusion fracture predicts the strength of the inclusions using $\sigma_G = K_{IC}/\sqrt{\pi a}$, which leads to $\sigma_G = 280$ MPa. This criterion also overestimates the actual strength of the inclusions in the staggered arrangement, by a factor of 3–7. These preliminary results highlight the need for an improved criterion for the fracture of the tablets. This criterion should take into account the presence of initial defects in the inclusions, as well as stress concentrations in the tablets. In particular, the way in which shear tractions are transmitted to the inclusions by the interfaces must be considered.

3. Shear transfer through the interfaces

The transfer of loads through the staggered structure can be represented by the well-known shear-tension chain, where the inclusions are in tension, and the interfaces are in shear [14]. Single inclusions are therefore subjected to shear traction from the interfaces as shown in figures 1b and 3a. These shear tractions are not necessarily uniform along the overlap region: in the case where the inclusions and interfaces are linear elastic, and the interface is thin compared with the inclusion, a simplified solution for the shear distribution along the interface is given by [29,30]:

$$\frac{\tau(x)}{\bar{\tau}} = \beta \frac{\cosh(\beta(2(x/L_o) - 1))}{\sinh \beta} \quad \text{with } \beta = \frac{L_o}{t}\sqrt{\frac{G_i}{E}\frac{t}{t_i}}, \quad (3.1)$$

where x is the position along the interface, t_i is the thickness of the interface, L_o and t are the overlap length and thickness of the inclusion (figure 3a), E is the tensile modulus of the inclusions and G_i is the shear modulus of the interface. $\bar{\tau}$ is the average shear stress along the overlap region, defined by

$$\bar{\tau} = \frac{1}{L_o}\int_0^{L_o} \tau(x)\,\mathrm{d}x = \frac{F}{2wL_o}. \quad (3.2)$$

This result is standard for shear lap configuration and staggered composites [15,17,27,29,30], but as opposed to previous work, we have defined the parameter β as a non-dimensional number, which makes it easier to interpret the model. The profile of shear stress along the interface (normalized by the average shear stress) for different values of β is shown in figure 3b. In general, the shear stress is not uniform and the stresses are concentrated at the ends of the interface
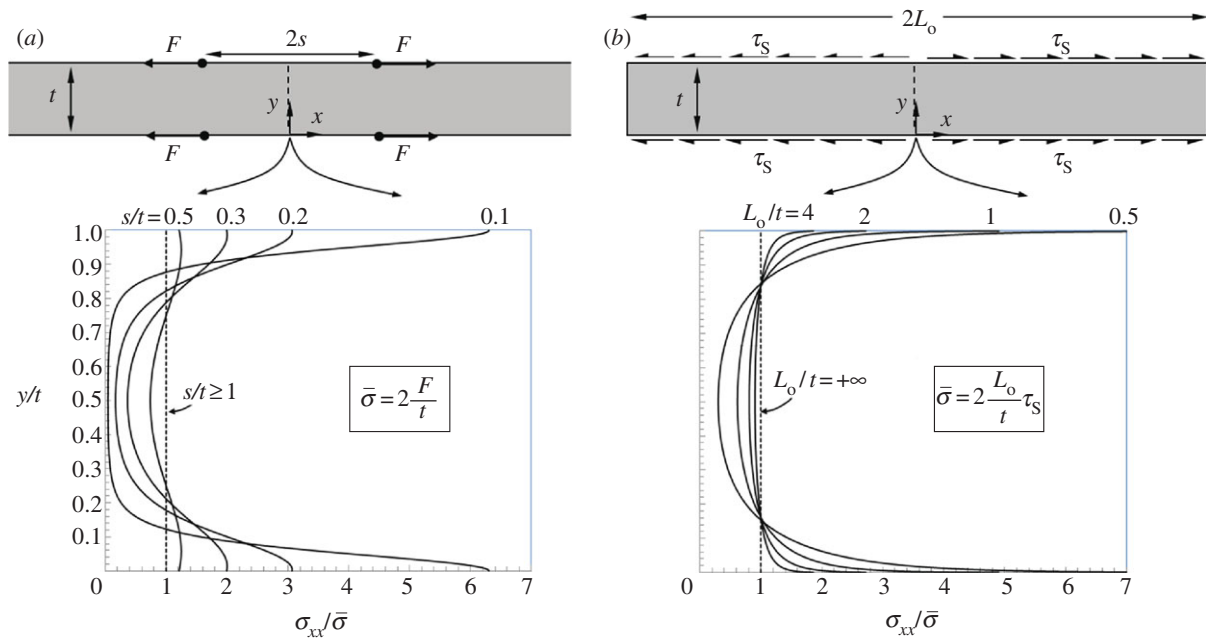
Figure 4. Normalized profiles of axial stress along the mid-section ($x = 0$) of an inclusion subjected to (a) two pairs of point forces spaced by $2s$ and (b) uniform shear tractions τ_S. (Online version in colour.)

region. This effect is more pronounced for higher values of β, corresponding to relatively stiff interfaces compared to the substrates (high $(G_i/E)(t/t_i)$ ratio) and/or longer normalized interface length (L_o/t). In the extreme case where $\beta = +\infty$, the shear tractions are only transferred near the ends of the interfaces while the tractions are zero anywhere else, so that the shear distribution may be represented by pairs of point forces (figure 3c). This extreme case will be used as a conservative case for the prediction of the failure of the inclusions. On the other hand, the shear stress is more uniform for small values of β, which correspond to relatively soft interfaces and/or short interface length. For $\beta = 0.4$ or lower, the shear stress deviates from its average value by 5 per cent at most. A uniform shear transfer to the inclusions was recently shown to be optimum because it maximizes the amount of elastic energy stored in the structure [27]. β is therefore the critical factor that determines how the shear is transferred through the interface. As an example, beta was evaluated for nacre in the elastic range of the interface. Using $L_o = 1\,\mu m$, $t = 500\,nm$, $t_i = 30\,nm$, $G_i = 0.8\,GPa$ and $E = 100\,GPa$ gives $\beta = 0.7$, representing an almost uniform shear stress along the overlap region.

The shear transfer model can be extended to the case where the interface undergoes plastic deformation. Once the ends of the interface reach the yield strength of an elastic–plastic interface, a plastic region appears and spreads towards the centre of the overlap region as the stress is increased [15]. Once the interface is entirely plastic and if perfect plasticity is assumed, the shear stress is uniform, which is equivalent to the case $\beta = 0$ described earlier. The distribution of shear tractions can therefore be summarized as follows: if the adhesive is elastic and much more compliant than the tablets and/or the overlap is short, then $\beta < 0.4$ and the shear tractions are uniformly distributed. This also applies to the case where the interface is fully plastic (assuming perfect plasticity) regardless of tablet properties and geometries. For all other cases (including cases where the interface exhibits strain hardening), the shear traction is non-uniform, the most extreme case being for $\beta = +\infty$,

where shear tractions can be represented by pairs of point forces applied at the ends of the overlap regions. In the rest of this article and in the criterion we propose, we do not incorporate the exact behaviour of the interface. Instead, we use its overall shear strength and we use β as a non-dimensional parameter which characterizes how the shear stress is transferred to the tablets. In this approach, the two extreme cases corresponding to $\beta = 0$ and $\beta = +\infty$ encompasses all possible geometry and constitutive laws for the interface.

4. Stress profiles in an inclusion subjected to shear tractions

We start by examining the problem of a two-dimensional elastic strip of thickness t and unit width subjected to two pairs of point forces as shown in figure 4a. The solution of this problem is obtained by superimposing the solutions provided by Cheng [31] for an elastic strip subjected to one pair of point forces (see appendix A for detailed results). The normalized stress along the mid-plane is displayed in figure 4a for different values of s. When the application points of these forces are far apart ($s/t \geq 1$) the stresses are uniform and equal to the average stress $\bar{\sigma} = 2F/t$. When the forces are applied closer to each other, the stresses concentrate near the surface of the tablets (at $y = 0$ and $y = t$) where they get substantially larger than $\bar{\sigma}$, while stresses deeper within the tablet approach zero. In the extreme case, s approaching zero leads to infinite stresses at ($x = 0$, $y = 0$) and ($x = 0$, $y = t$).

The stress profile due to a uniform shear traction (figure 4b) can now be calculated by simply integrating the previous result over a length L_o along the inclusions (appendix A). The resulting stress profiles are shown in figure 4b. The results show very high stresses near the surfaces of the inclusions, and singularities at the points of coordinates (0, 0) and (0, t), for all values of L_o/t. Within the tablets, the stresses are more uniformly distributed for large overlap ratio L_o/t, approaching a uniform distribution for $L_o/t = +\infty$. These results are identical
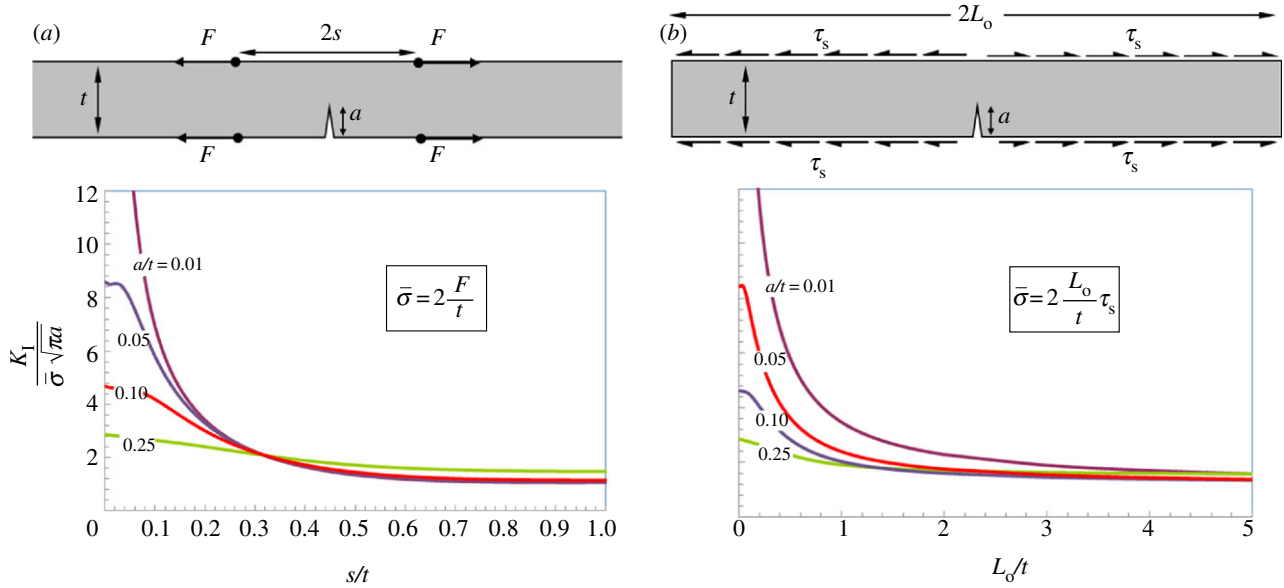
Figure 5. Normalized stress intensity factors for a cracked inclusion subjected to (a) two pairs of point forces spaced by 2s and (b) uniform shear tractions. (Online version in colour.)

to those calculated in previous work using finite elements and cohesive elements to simulate the interface [22]. Predicting the failure of the inclusion in this case is difficult because of the stress singularities. A failure criterion based on fracture mechanics may be more appropriate, considering that the singularities occurs because of the junctions at the ends of the tablets, which act as crack-like features. The fracture problem is however not well-defined, because the order of the singularity is not exactly $\frac{1}{2}$.

5. Stress intensity factors in cracked inclusions

The presence of pre-existing flaws within the inclusions is more realistic and should be taken into account for a brittle material. In particular, we focus on an edge crack located at $x = 0$ because it is where the stresses are the highest, and where fracture occurred in the experiments presented earlier. The stress intensity factor resulting from two pairs of point forces is shown in figure 5a (equations are given in appendix B). The stress intensity factor reaches high values for small s, consistent with the higher local stresses generated when the pair of point forces are close to each other (figure 5a). This effect is more pronounced for shorter cracks, because the crack tip is closer to the regions of high stresses generated by the point forces (figure 4a). For larger values of s/t, the normalized stress intensity factor decreases and converges towards the solution for an edge crack under uniform tension.

We can now integrate this result over the overlap length to obtain the stress intensity factor resulting from applied shear tractions (figure 5b):

$$\frac{K_{\mathrm{I}}}{\bar{\sigma}\sqrt{\pi a}} = \int_{(x/L_{\mathrm{o}})=0}^{1} \frac{K_{\mathrm{I}}^{(\mathrm{F})}}{(2F/t)\sqrt{\pi a}} \frac{\tau(x)}{\bar{\tau}} \mathrm{d}\left(\frac{x}{L_{\mathrm{o}}}\right), \qquad (5.1)$$

where $\bar{\sigma} = 2(L_{\mathrm{o}}/t)\bar{\tau}$ and $\bar{\tau} = $ average shear stress applied. In the case where the shear stress is uniform ($\tau(x)/\bar{\tau} = 1$) in equation (5.1). The normalized stress intensity factor for this case is plotted in figure 5b, as function of overlap ratio (L_{o}/t). The overall response is similar to figure 5a. The stress intensity factor is larger for small aspect ratios, especially for (L_{o}/t) < 2, and this effect is more pronounced for relatively short cracks

(small a/t). For a large aspect ratio, the stress intensity approaches the solution for an edge crack in an infinite plate subjected to uniaxial tension. This result has important implications in terms of material design. The strength of the staggered composite is given by the simple relation:

$$\sigma_{\mathrm{S}} = \frac{L_{\mathrm{o}}}{t}\tau_{\mathrm{S}}. \qquad (5.2)$$

In terms of material design, this equation shows that the tensile strength can be increased by either increasing the overlap ratio L_{o}/t or by increasing the shear strength of the interface τ_{S}. Our new failure criterion predicts that increasing the overlap ratio is a better approach because it tends to reduce the stress intensity factor and the likelihood of tablet fracture. In the case of non-uniform shear tractions ($\beta > 0.4$), the tractions near the ends of the overlap regions are larger, with the effect of increasing the stress intensity factor. In the most extreme case ($\beta = +\infty$), the shear tractions are represented by pairs of point forces, and the corresponding stress intensity factor can be computed by combining the solution of two pairs of point force for the case $s = 0$ superimposed with the case $s = +\infty$. This solution is clearly the worst case scenario in terms of load transfer, and will be used as a conservative approach in the design of the microstructure for cases where the shear traction profile is not known. Finally, we note that while the results above were developed for a symmetric case where $L_{\mathrm{o}} = L/2$, they can also be used for asymmetric or random microstructure because the force transmitted by shear via the interfaces is uniform throughout the structure. For asymmetric cases, the shorter of the two overlap lengths should be considered as L_{o} for failure prediction.

6. New failure criterion and design optimization

We now apply the solutions developed above to the actual design optimization of staggered inclusions. The stress intensity factor from equation (5.1) can be written in the following form:

$$\frac{K_{\mathrm{I}}}{\bar{\sigma}\sqrt{\pi a}} = f\left(\frac{a}{t}, \frac{L_{\mathrm{o}}}{t}\right). \qquad (6.1)$$
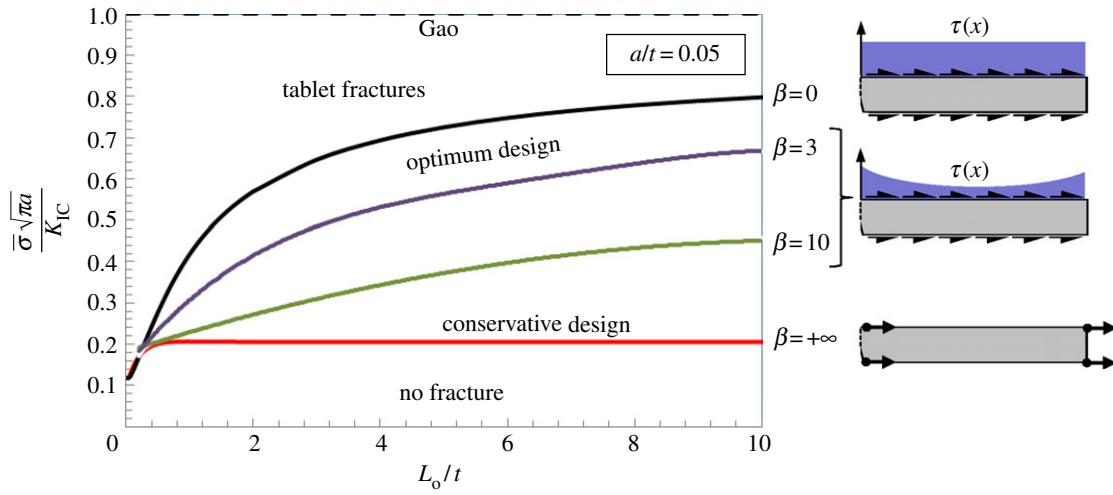
Figure 6. Illustration of the failure criteria for the case of a short edge crack: $a/t = 0.05$. (Online version in colour.)
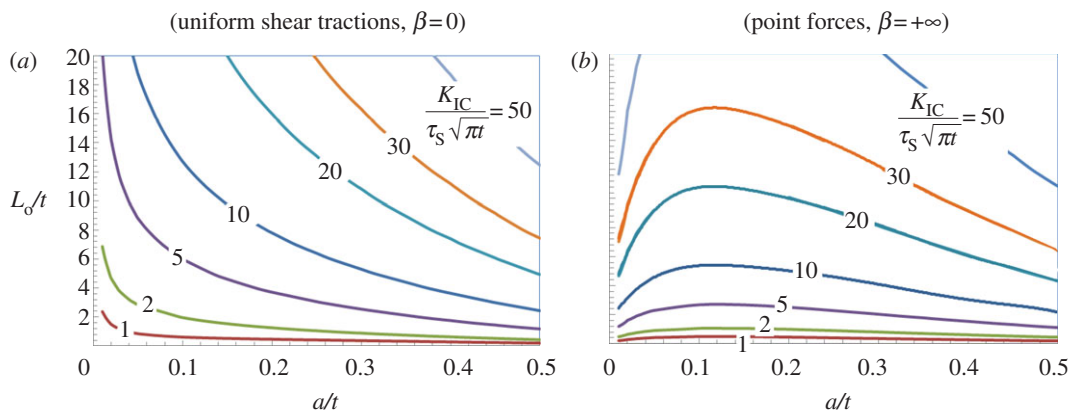

Figure 7. Design spaces for (a) optimum and (b) conservative designs. For a given value of $K_{IC}/\tau_S\sqrt{\pi t}$, the inclusions will slide for combinations of $\{a/t, L_o/t\}$ below the corresponding curve, and they will fracture for combinations above the curve. (Online version in colour.)

In order to prevent tablet fracture, one must have $K_I < K_{IC}$, which leads to:

$$\frac{\bar{\sigma}\sqrt{\pi a}}{K_{IC}} < \frac{1}{f\,(a/t), (L_o/t)}. \qquad (6.2)$$

This expression can now be used to determine the maximum average stresses that the tablets can withstand before failure. This criterion is illustrated in figure 6 for the case of a short edge crack ($a/t = 0.05$). The optimum design is the case where the shear tractions are uniform ($\beta = 0$), which corresponds to the most efficient shear transfer. In this case, higher stresses can be achieved for longer overlap ratio L_o/t. The conservative design is based on shear transfer by point forces ($\beta = +\infty$). This is a worst case situation in terms of shear transfer, and the model predicts, as expected, a lower maximum stress. In the conservative case, the fracture of the inclusion becomes independent from L_o/t for $L_o/t > 0.6$. This specific criterion is appropriate if the shear traction distribution is not known for the materials at hand. Intermediate states ($\beta = 3, \beta = 10$) are also shown in figure 6. Finally, Gao's simplified failure criterion is found by letting $f\,(a/t), (L_o/t) = 1$, which clearly overestimates the load-carrying capabilities of the inclusions (figure 6).

Alternatively, and perhaps more conveniently for design purposes, the failure criterion may be expressed as function of the shear strength of the interface τ_S:

$$2\frac{L_o}{t}\sqrt{\frac{a}{t}}f\left(\frac{a}{t}, \frac{L_o}{t}\right) < \frac{K_{IC}}{\tau_S\sqrt{\pi t}}. \qquad (6.3)$$

Once the non-dimensional number $K_{IC}/\tau_S\sqrt{\pi t}$ and the initial flaw size are determined for a given set of components and a given length scale of the microstructure, equation (6.3) can be used to compute the maximum overlap ratio that will prevent tablet fracture. A graphical representation of this criterion is shown for the optimum design (figure 7a) and the conservative design (figure 7b). The lower section of these graphs represents regions where the tablets will pull out while the upper sections represent regions where the tablets will fracture. The transition line between the two failure models depends on the value of $K_{IC}/\tau_S\sqrt{\pi t}$. Tougher inclusions, weaker interfaces and smaller inclusion size thereby expand the range of possible values for overlap ratio and tolerable flaw size. In general, smaller initial defects allow for a greater overlap ratio, except for the conservative design case, where cracks shorter than $a/t < 0.15$ are detrimental because the crack tip interacts with the high stresses generated by the point forces at the crack mouth. For long cracks $a/t > 0.5$, the optimum and conservative approaches lead to the same results: uniform tractions or point forces have the same effect on the crack tip if it is far enough
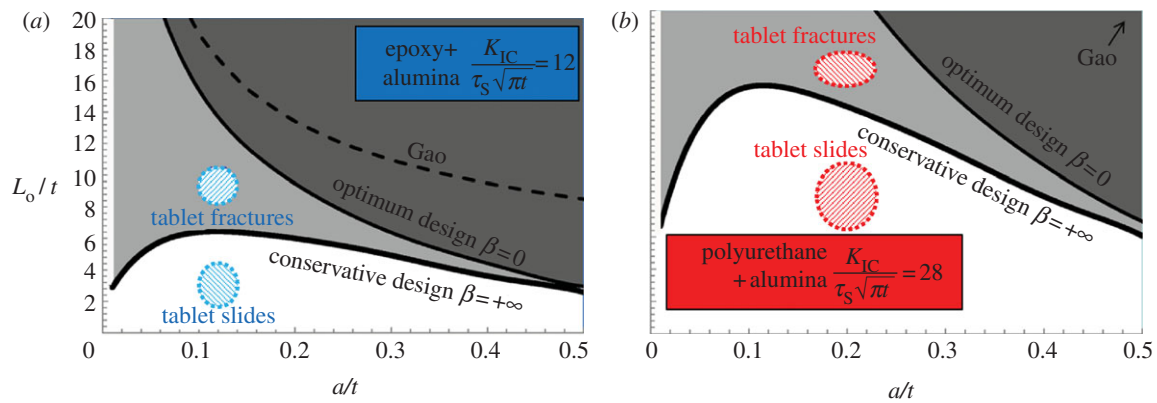
Figure 8. Comparison of the existing (Gao) and the new failure criteria with actual experiments for (a) epoxy on alumina and (b) polyurethane on alumina. (Online version in colour.)
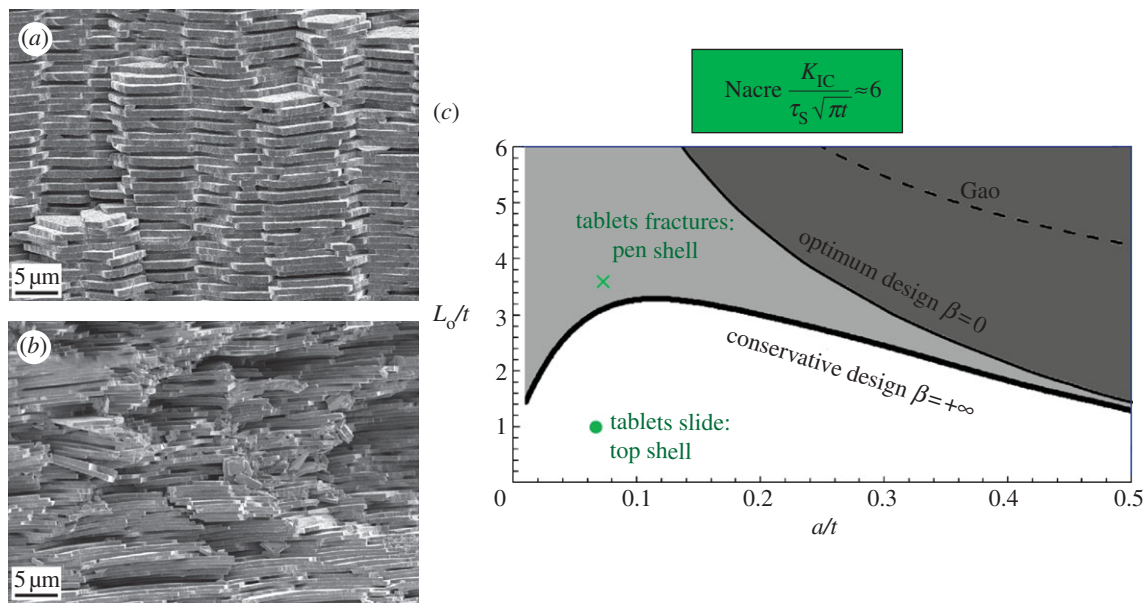

Figure 9. Scanning electron micrographs of fracture surface for (a) nacre from top shell and (b) nacre from pen shell; (c) comparison of existing (Gao) and new failure criteria with experimental data for these two types of nacre. (Online version in colour.)

from the surfaces (in other words any one of these two types of load is 'perceived' as a remote load by the crack tip).

This new criterion can now be compared with the experiments on alumina tablets presented above. Using $K_{IC} = 3.9$ MPa.m$^{1/2}$ and $t = 0.5$ mm for the alumina tablets and $\tau_S = 8.2$ MPa gives $K_{IC}/\tau_S\sqrt{\pi t} = 12$ for the alumina/epoxy structure, which is illustrated in figure 8a. Using $K_{IC} = 3.9$ MPa.m$^{1/2}$ and $t = 0.3$ mm for the alumina tablets and $\tau_S = 4.5$ MPa gives $K_{IC}/\tau_S\sqrt{\pi t} = 28$ the alumina/polyurethane structure, illustrated in figure 8b. For both cases, an initial flaw size of $a = 60$ μm was used as determined earlier. For the epoxy and polyurethane interfaces, exact values for β are difficult to obtain: Epoxy strain hardens upon yielding, and polyurethane displays nonlinear elastic behaviour. The two criteria (optimum and conservative) are therefore shown. Figure 8 shows that our new failure criterion properly predicts the fracture and survival of the alumina inclusions for the case of epoxy and polyurethane, depending on the overlap ratio. For both adhesives, structures with short aspect ratios are located in the white area of the design space, representing the area where the tablets remain intact and the system fail by pullout. Experimental data with longer aspect ratios fall in the light grey area, where fracture of the tablets depends on the exact value of β. In this case, a

conservative version of the failure criterion captures the transition from pullout to tablet fracture properly. The failure criterion therefore represents a significant improvement over existing criteria, which can be further refined if the exact distribution of shear traction on the tablets is known.

Finally, the predictions of the new criterion are compared with nacre. Nacre from top shell (*Trochus niloticus*) predominantly fails by pullout of the tablets (figure 9a), which is typical to the type of nacre discussed in the literature. Imaging and analysis of this type of nacre revealed an average overlap ratio of $L_o/t = 1.2$. We also have identified another type of nacre, from pen shell (*Pinna nobilis*) for which the fracture of tablets is prominent (figure 9b). The fragility of this type of shell is known to shell collectors but the evolutionary causes for the lower performance of this type of nacre are unknown. It is possible that pen shell grows nacre of lower performance because it benefits from another protection: pen shell partially buries itself in sandy areas. Image analysis of the pen shell nacreous layer revealed an overlap ratio of $L_o/t = 3.6$. For both types of nacres, we take the initial flaw size as the size of the nanograins within the tablets ($a \approx 40$ nm [32]), assuming that potential flaws occupy a grain boundary. Using $K_{IC} = 0.39$ MPa.m$^{1/2}$ [33], $t \approx 500$ nm for the mineral tablets and $\tau_S = 50$ MPa [20] gives $K_{IC}/\tau_S\sqrt{\pi t} \approx 6$.

Once again the exact value of β is not known because of strain hardening at the interface, and therefore both conservative and optimum criteria are considered. Figure 9c shows the failure criterion and the experimental data from the two types of nacre. The conservative form of the new criterion predicts the behaviour of the tablets remarkably well, considering the complex three-dimensional arrangement of natural nacre.

7. Conclusions

The staggered composite structure generates unique combinations of strength and toughness in natural materials. Existing models show that the performance of this type of composite increases when the overlap between inclusions is increased, at the expense of higher stresses carried the inclusions and potential fracture of the inclusions themselves. This failure mode is highly detrimental, and it must be considered and predicted in the design of engineered, bio-inspired staggered composites. In this work, we have developed the most accurate failure criterion to date for the prediction of inclusion fracture. The state of stress within the inclusion is highly dependent on the way shear tractions are transmitted to the inclusions, which is controlled by a single parameter β. An 'optimum' form of the criterion is given where the shear tractions are transferred to the inclusions uniformly ($\beta = 0$). For cases where the shear load transfer is not well known, a 'conservative' criterion is also provided (case $\beta = +\infty$). This approach is general enough to be applied to any material or geometry at the interface. Capturing the exact failure transition between the sliding and the fracture of the tablet would require a large number of additional tests to take into account the statistics associated with flaw distribution in the ceramic or mineral tablets, and the result would be geometry- and adhesive-specific. Our new criterion successfully predicts the failure of millimetre-size alumina tablets bonded by engineering glues, as well as the failure or survival of mineral tablets in pen shell and top shell nacres. The criterion also yields useful design guidelines. For example, large overlap with weak interfaces should be preferred over short overlaps with strong interfaces in order to minimize the risk of tablet fracture. While the model only considers the case where the overlap is half of the length of the inclusions, the criterion also applies for any other overlap length $L_o < L/2$. In terms of size effects, as emphasized in a previous work [24], nanoscale inclusions have the highest strength because they become insensitive to the presence of flaws. Our criterion is consistent with this finding, but in addition it enables predictions and designs at larger scales, where initial flaws must be considered. This is relevant for nacre or, for example, freeze cast materials [13], which are two of the most successful natural and engineered staggered structures that are both made of microscale inclusions. The criterion can also be applied to even larger microstructures in the order of millimetres [12,34]. It can finally be applied over several length scales simultaneously, to design and optimize hierarchical materials with staggered arrangements used over two or more levels of hierarchy [25].

Appendix A. Stress distribution along the midline of an elastic strip subjected to a pair of point forces

The solution developed by Cheng et al. [31] for one pair of forces can be superimposed to find the stress profile for two pairs of forces (as shown in figure 4):

$$\sigma_{yy}^{(F)}(\tilde{x}, 0) = \frac{F}{\pi t} 4\tilde{s}^3 \left[\frac{1}{(\tilde{s}^2 + \tilde{x}^2)^2} + \frac{1}{(\tilde{s}^2 + (1 - \tilde{x})^2)^2} \right]$$

$$+ \int_0^\infty \{(1 - \alpha)G(\alpha, \tilde{x}) + \alpha H(\alpha, \tilde{x})\} e^{-\alpha} \sin \alpha \tilde{s} \, d\alpha, \quad \text{(A 1)}$$

with $\tilde{x} = x/t$, $\tilde{s} = s/t$ and

$$\left. \begin{array}{l} G(\alpha, \tilde{x}) = 2 \dfrac{\alpha(1 - \tilde{x}) \sinh \alpha \tilde{x} - 2 \cosh \alpha(1 - \tilde{x}) + \alpha \tilde{x} \sinh \alpha(1 - \tilde{x}) - 2 \cosh \alpha \tilde{x}}{\sinh \alpha + \alpha} \\[2ex] \text{and} \quad H(\alpha, \tilde{x}) = 2 \dfrac{\alpha(1 - \tilde{x}) \cosh \alpha \tilde{x} - 2 \sinh \alpha(1 - \tilde{x}) + \alpha \tilde{x} \cosh \alpha(1 - \tilde{x}) - \sinh \alpha \tilde{x}}{\sinh \alpha + \alpha} \end{array} \right\} . \quad \text{(A 2)}$$

It is convenient to define the average stress along the midline plane ($x = 0$) as:

$$\bar{\sigma} = \frac{1}{t} \int_0^t \sigma_{xx}(0, y) \, dy. \quad \text{(A 3)}$$

The stress profile due to a uniform shear traction (as shown in figure 4b) can now be calculated by simply integrating the previous result over a length L_o along the inclusions:

$$\sigma_{xx}^{(\tau)}(\tilde{x}, 0) = \int_0^{L_o} \frac{\sigma_{xx}^{(F)}(\tilde{x}, 0)}{F} \tau \, dx. \quad \text{(A 4)}$$

Appendix B. Stress intensity factors for an edge crack in an elastic strip subjected to point forces, and to shear tractions

Following Cheng et al. [31], an edge crack is introduced on the strip by imposing tractions to enforce the free surfaces on the crack faces. We focus on the resulting stress intensity factor at the edge crack (shown in figure 5a), which can be written [31] as:

$$K_I = f_o \sqrt{\pi a} \int_0^{a/t} \frac{2}{\pi} \left[(1 - \tilde{x})(2 + h - 3hx) \cos^{-1}\left(\frac{gx}{1 - x}\right) \right.$$

$$\left. + g(1 - hx)\left(1 - \left(\frac{gx}{1 - x}\right)^2\right)^{1/2} \right] \sigma_{yy}(\tilde{x}, 0) \, d\tilde{x}. \quad \text{(B 1)}$$

Where g and h are functions of a/t:

$$g(a/t) = (1 - a/t)/(a/t)$$

$$h(a/t) = (3/28)(1 - 7a/t)(1 - a/t)^5/(a/t) \qquad (B\,2)$$

And f_o is the traditional correction factor for an edge crack (valid for $a/t \leq 0.6$):

$$f_o\left(\frac{a}{t}\right) = 1.12 - 0.23\left(\frac{a}{t}\right)$$
$$+ 10.6\left(\frac{a}{t}\right)^2 - 21.8\left(\frac{a}{t}\right)^3 + 30.4\left(\frac{a}{t}\right)^4. \qquad (B\,3)$$

We can now integrate this result over the overlap length to obtain the stress intensity factor resulting from applied shear tractions (figure 5b):

$$\frac{K_{\mathrm{I}}}{\bar{\sigma}\sqrt{\pi a}} = \int_{(x/L_o)=0}^{1} \frac{K_{\mathrm{I}}^{(F)}}{(2F/t)\sqrt{\pi a}} \frac{\tau(x)}{\bar{\tau}} \mathrm{d}\left(\frac{x}{L_o}\right), \qquad (B\,4)$$

where $\bar{\sigma} = 2(L_o/t)\bar{\tau}$ and $\bar{\tau}$ = average shear stress applied. In the case where the shear stress is uniform $(\tau(x))/(\bar{\tau}) = 1$ in equation (B 4).

References

1. Ashby MF. 2005 Hybrids to fill holes in material property space. *Philos. Mag.* **85**, 3235–3257. (doi:10.1080/14786430500079892)

2. Jäger I, Fratzl P. 2000 Mineralized collagen fibrils: a mechanical model with a staggered arrangement of mineral particles. *Biophys. J.* **79**, 1737–1746. (doi:10.1016/S0006-3495(00)76426-5)

3. Keten S, Xu ZP, Ihle B, Buehler MJ. 2010 Nanoconfinement controls stiffness, strength and mechanical toughness of beta-sheet crystals in silk. *Nat. Mater.* **9**, 359–367. (doi:10.1038/nmat2704)

4. Fratzl P, Misof K, Zizak I, Rapp G, Amenitsch H, Bernstorff S. 1998 Fibrillar structure and mechanical properties of collagen. *J. Struct. Biol.* **122**, 119–122. (doi:10.1006/jsbi.1998.3966)

5. Currey JD. 1977 Mechanical properties of mother of pearl in tension. *Proc. R. Soc. Lond. B* **196**, 443–463. (doi:10.1098/rspb.1977.0050)

6. Gao HJ. 2006 Application of fracture mechanics concepts to hierarchical biomechanics of bone and bone-like materials. *Int. J. Fracture* **138**, 101–137. (doi:10.1007/s10704-006-7156-4)

7. Ritchie RO. 2011 The conflicts between strength and toughness. *Nat. Mater.* **10**, 817–822. (doi:10.1038/nmat3115)

8. Barthelat F, Rabiei R. 2011 Toughness amplification in natural composites. *J. Mech. Phys. Solids* **59**, 829–840. (doi:10.1016/j.jmps.2011.01.001)

9. Shao Y, Zhao HP, Feng XQ, Gao H. 2012 Discontinuous crack-bridging model for fracture toughness analysis of nacre. *J. Mech. Phys. Solids* **60**, 1400–1419. (doi:10.1016/j.jmps.2012.04.011)

10. Tang ZY, Kotov NA, Magonov S, Ozturk B. 2003 Nanostructured artificial nacre. *Nat. Mater.* **2**, 413–418. (doi:10.1038/nmat906)

11. Bonderer LJ, Studart AR, Gauckler LJ. 2008 Bioinspired design and assembly of platelet reinforced polymer films. *Science* **319**, 1069–1073. (doi:10.1126/science.1148726)

12. Barthelat F, Zhu DJ. 2011 A novel biomimetic material duplicating the structure and mechanics of natural nacre. *J. Mater. Res.* **26**, 1203–1215. (doi:10.1557/jmr.2011.65)

13. Deville S, Saiz E, Nalla RK, Tomsia AP. 2006 Freezing as a path to build complex composites. *Science* **311**, 515–518. (doi:10.1126/science.1120937)

14. Fratzl P, Gupta HS, Paschalis EP, Roschger P. 2004 Structure and mechanical quality of the collagen-mineral nano-composite in bone. *J. Mater. Chem.* **14**, 2115–2123. (doi:10.1039/b402005g)

15. Kotha SP, Li Y, Guzelsu N. 2001 Micromechanical model of nacre tested in tension. *J. Mater. Sci.* **36**, 2001–2007. (doi:10.1023/A:1017526830874)

16. Begley MR, Philips NR, Compton BG, Wilbrink DV, Ritchie RO, Utz M. 2012 Micromechanical models to guide the development of synthetic 'brick and mortar' composites. *J. Mech. Phys. Solids* **60**, 1545–1560. (doi:10.1016/j.jmps.2012.03.002)

17. Wei XD, Naraghi M, Espinosa HD. 2012 Optimal length scales emerging from shear load transfer in natural materials: application to carbon-based nanocomposite design. *ACS Nano* **6**, 2333–2344. (doi:10.1021/nn204506d)

18. Gupta HS, Seto J, Wagermaier W, Zaslansky P, Boesecke P, Fratzl P. 2006 Cooperative deformation of mineral and collagen in bone at the nanoscale. *Proc. Natl Acad. Sci. USA* **103**, 17 741–17 746. (doi:10.1073/pnas.0604237103)

19. Wang RZ, Suo Z, Evans AG, Yao N, Aksay IA. 2001 Deformation mechanisms in nacre. *J. Mater. Res.* **16**, 2485–2493. (doi:10.1557/JMR.2001.0340)

20. Barthelat F, Tang H, Zavattieri PD, Li CM, Espinosa HD. 2007 On the mechanics of mother-of-pearl: a key feature in the material hierarchical structure. *J. Mech. Phys. Solids* **55**, 225–444. (doi:10.1016/j.jmps.2006.08.002)

21. Jackson AP, Vincent JFV, Turner RM. 1988 The mechanical design of nacre. *Proc. R. Soc. Lond. B* **234**, 415–440. (doi:10.1098/rspb.1988.0056)

22. Bekah S, Rabiei R, Barthelat F. 2011 Structure, scaling, and performance of natural micro- and nanocomposites. *BioNanoScience* **1**, 53–61. (doi:10.1007/s12668-011-0008-3)

23. Ji BH, Gao HJ. 2004 A study of fracture mechanisms in biological nano-composites via the virtual internal bond model. *Mater. Sci. Eng. A* **366**, 96–103. (doi:10.1016/j.msea.2003.08.121)

24. Gao HJ, Ji BH, Jager IL, Arzt E, Fratzl P. 2003 Materials become insensitive to flaws at nanoscale: lessons from nature. *Proc. Natl Acad. Sci. USA* **100**, 5597–5600. (doi:10.1073/pnas.0631609100)

25. Zhang ZQ, Zhang YW, Gao HJ. 2011 On optimal hierarchy of load-bearing biological materials. *Proc. R. Soc. B* **278**, 519–525. (doi:10.1098/rspb.2010.1093)

26. ASTM. 2008 *Standard test method for strength properties of double lap shear adhesive joints by tension loading, ASTM Standard D3528–96*. West Conshohocken, PA: ASTM International.

27. Chen B, Wu PD, Gao H. 2009 A characteristic length for stress transfer in the nanostructure of biological composites. *Compos. Sci. Technol.* **69**, 1160–1164. (doi:10.1016/j.compscitech.2009.02.012)

28. Tada H, Paris PC, Irwin GR, Engineers ASoM. 2000 *The stress analysis of cracks handbook*, vol. 130. New York, NY: ASME press.

29. Tsai MY, Oplinger DW, Morton J. 1998 Improved theoretical solutions for adhesive lap joints. *Int. J. Solids Struct.* **35**, 1163–1185. (doi:10.1016/S0020-7683(97)00097-8)

30. Volkersen O. 1938 Die Nietkraftverteilung in zugbeanspruchten Nietverbindungen mit konstanten Laschen-guerschnitten. *Luftfahrtforschung* **15**, 41–47.

31. Cheng W, Finnie I, Vardar O. 1992 Deformation of an edge-cracked strip subjected to normal surface traction on the crack faces. *Eng. Fracture Mech.* **42**, 97–107. (doi:10.1016/0013-7944(92)90281-I)

32. Rousseau M, Lopez E, Stempfle P, Brendle M, Franke L, Guette A, Naslain R, Bourrat X. 2005 Multiscale structure of sheet nacre. *Biomaterials* **26**, 6254–6262. (doi:10.1016/j.biomaterials.2005.03.028)

33. Broz ME, Cook RF, Whitney DL. 2006 Microhardness, toughness, and modulus of Mohs scale minerals. *Am. Miner.* **91**, 135–142. (doi:10.2138/am.2006.1844)

34. Espinosa HD, Juster AL, Latourte FJ, Loh OY, Gregoire D, Zavattieri PD. 2011 Tablet-level origin of toughening in abalone shells and translation to synthetic composite materials. *Nat. Commun.* **2**, 173. (doi:10.1038/ncomms1172)